

## SIMULATING TIDAL STREAMS IN A HIGH-RESOLUTION DARK MATTER HALO

WAYNE NGAN<sup>1</sup>, BRANDON BOZEK<sup>2,3</sup>, RAYMOND G. CARLBERG<sup>1</sup>, ROSEMARY F. G. WYSE<sup>3</sup>, ALEXANDER S. SZALAY<sup>3</sup>, PIERO MADAU<sup>4</sup>

<sup>1</sup> Department of Astronomy and Astrophysics, University of Toronto, Toronto, ON, M5S 3H4, Canada

<sup>2</sup> Department of Astronomy and Joint Space-Science Institute, University of Maryland, College Park, MD, 20742, USA

<sup>3</sup> Department of Physics and Astronomy, The Johns Hopkins University, Baltimore, MD, 21218, USA

<sup>4</sup> Department of Astronomy and Astrophysics, University of California, Santa Cruz, CA, 95064, USA

*Draft version June 9, 2021*

### ABSTRACT

We simulate tidal streams in the presence and absence of substructures inside the zero-redshift snapshot of the Via Lactea II (VL-2) simulation. A halo finder is used to remove and isolate the subhalos found inside the high-resolution dark matter halo of VL-2, and the potentials for both the main halo and all the subhalos are constructed individually using the self-consistent field (SCF) method. This allows us to make direct comparison of tidal streams between a smooth halo and a lumpy halo without assuming idealized profiles or triaxial fits. We simulate the kinematics of a star cluster starting with the same orbital position but two different velocities. Although these two orbits are only moderately eccentric and have similar apo- and pericentric distances, we find that the two streams have very different morphologies. We conclude that our model of the potential of VL-2 can provide insights about tidal streams that have not been explored by previous studies using idealized or axisymmetric models.

*Subject headings:* dark matter — galaxies: dwarf — galaxies: interactions — Galaxy: kinematics and dynamics

### 1. INTRODUCTION

In the  $\Lambda$ CDM hierarchical structure formation model, smaller structures form first and merge to form larger structures (Blumenthal et al. 1984; Davis et al. 1985; Bardeen et al. 1986). This process is not complete; many of the smaller structures survive until today to become substructures within larger structures like the Milky Way. This has been demonstrated by high-resolution simulations of Milky-Way-sized dark matter halos, which are populated by numerous subhalos (Diemand et al. 2007, 2008; Madau et al. 2008; Springel et al. 2008; Stadel et al. 2009; Zemp 2009; Gao et al. 2011). On the other hand, the observed abundances of satellite galaxies around the Milky Way or M31 are much lower than the abundances of subhalos predicted by simulations. This disagreement between observation and theory is commonly known as the missing satellite problem (Klypin et al. 1999; Moore et al. 1999; Strigari et al. 2007).

Tidal streams, or remnants of stellar structures as they are tidally disrupted by a massive host, are powerful probes for the potential in the the Milky Way (e.g., Johnston 1998; Helmi et al. 2003; Law et al. 2005). If subhalos exist, they should interact with the stream dynamically and leave detectable signatures along the stream. Ibata et al. (2002) first simulated a globular cluster in idealized galaxy potentials both with and without subhalos and found that the resulting streams had distinguishable kinematics when subhalos were present. More recently, both idealized simulations (Yoon et al. 2011; Carlberg 2012) and self-gravitating simulations (Erkal & Belokurov 2014; Ngan & Carlberg 2014) found that a close encounter between a subhalo

and a stream can produce a “gap” which can be observed as an underdensity of stars along the stream. In particular, Carlberg et al. (2012), Carlberg (2012), and Carlberg & Grillmair (2013) analytically derived the gap formation rate as an observable quantity, so the number of gaps can be a powerful probe for the abundance of subhalos.

Detailed observations of densities along stellar streams show that streams have many longitudinal underdensities (Carlberg et al. 2011, 2012; Carlberg & Grillmair 2013), but some studies have found that intrinsic mechanisms such as epicyclic overdensities (EOs; Küpper et al. 2008, 2010, 2012) and Jeans instabilities (Comparetta & Quillen 2011) can also produce gap-like features which can be confused with gaps induced by subhalo perturbations. Ngan & Carlberg (2014, hereafter NC14) simulated streams in identical orbits with and without subhalos and concluded that EO gaps can be distinguished from subhalo gaps by the locations and the size distribution of the gaps.

All of the above simulations share the same limitation — idealized dark matter halo profiles. Navarro et al. (1997, 2004, 2010) showed that dark matter halos can be described by universal profiles such as Navarro-Frenk-White and Einasto profiles, and the former is used by some simulations mentioned above because of its simple form. However, idealized profiles are spherically averaged best-fit results, which do not capture the shape of the halo. Both N-body simulations (Jing & Suto 2002; Zemp et al. 2009) and the results inferred from observations of the Milky Way (Law et al. 2009) show that halos are not spherical. Siegal-Gaskins & Valluri (2008) simulated the disruption of a satellite galaxy and its resulting stream in a flattened potential both with and without substructures, and they found that even though

substructures make the stream more clumpy, the shape of the halo has a larger effect on the satellite’s disruption than substructures have. Nevertheless, their underlying halo potential still follows an idealized profile, and their stream progenitor is much more massive than the streams we consider in this study. In this study, we focus on the disruption of a globular cluster in a realistic potential of a Milky-Way-sized dark matter halo in both the presence and absence of substructures, without using idealized profiles in either case. The realistic potential is constructed from the zero-redshift snapshot of the Via Lactea II (VL-2) simulation, which simulated the formation of a Milky-Way-sized dark matter halo using more than  $10^9$  particles (or about  $4.1 \times 10^3 M_\odot$  per particle) in the  $\Lambda$ CDM cosmological context starting from redshift  $z = 104$  (Diemand et al. 2008).

The goal of this study is to demonstrate the difference in the appearance of tidal streams in two cases: (1) a “smooth” dark matter halo without subhalos, and (2) a “lumpy” dark matter halo with the amount of substructures expected in a  $\Lambda$ CDM cosmology. Our simulation parameters are chosen so that the resulting streams would be comparable to GD-1 (Grillmair & Dionatos 2006), a dynamically cold and narrow stream observed in the Milky Way. Our simulations are not meant to be physical models of GD-1, though, because VL-2 is not a physical model of the the Milky Way, and we are only constructing a time-independent potential using one snapshot at redshift zero of VL-2. The details of orbital or stream dynamics in the VL-2 potential are beyond the scope of this study, as they are complicated topics that warrant much more focused studies in the future. This study is meant to present the method to construct realistic dark matter halo potentials in the presence and absence of substructures requiring neither idealized profiles nor triaxial fits. This allows us to isolate and investigate the effects that substructures have on a GD-1-like stream in a more realistic setting than in NC14.

Since the tidal disruption of a star cluster is an ongoing process that lasts as long as the formation of the dark matter halo itself, a redshift-dependent potential using all available snapshots of VL-2 is our goal in the future. Bonaca et al. (2014) approached this by using a “live” halo, which essentially resimulated VL-2 but approximated the formation of streams. Another advantage of a live halo is that it can respond to an external system in order to account for effects such as dynamical friction. On the other hand, a live halo may be computationally expensive depending on its resolution. We did not use a live halo because our goal is not to rerun VL-2, but to construct a realistic model of the existing VL-2 halo at arbitrarily high accuracy and use this model as a background for our own N-body simulations. Moreover, our streams’ masses are low enough that they will not affect the evolution of the halo, and dynamical friction is negligible (NC14).

This paper is organized as follows. Section 2 describes the method of using the self-consistent field (SCF) method to construct the potential of VL-2, which is done after identifying the subhalo particles using a halo finder. Section 3 summarizes the parameters for our simulations such as our choice of orbits. Section 4 is the key part of this study, which presents the goodness of the SCF, as well as the details of the simulated streams. Section 5

summarizes our results.

## 2. METHOD

### 2.1. SCF Method

Originally developed to compute collisionless N-body dynamics for galaxies (Hernquist & Ostriker 1992), the SCF method solves the gravitational Poisson equation by basis decomposition. This method is optimized for dark matter halos since its lowest-order basis function is already an idealized profile, and the higher-order basis functions can be used to describe the radial and angular deviations from this idealized profile. The basis functions are bi-orthonormal and complete, so they can model any matter distribution as the decomposition order increases.

The approach to model the gravitational potentials in the snapshots of existing simulations of dark matter halos has been studied extensively by Lowing et al. (2011, hereafter L11). Even with moderate decomposition orders, L11 was able to recover much of the detailed dynamics inside the halos of the Aquarius simulations (Springel et al. 2008). We follow their approach to compute the forces in the halo of the VL-2 simulation at redshift zero. In this section we briefly summarize the method.

The density  $\rho(\mathbf{r})$  and gravitational potential  $\Phi(\mathbf{r})$  are related by the Poisson equation  $\nabla^2 \Phi = 4\pi G\rho$ . Given a simulation snapshot that contains  $\rho$ , SCF solves the Poisson equation by decomposing  $\Phi$  and  $\rho$  such that

$$\Phi(\mathbf{r}) = \sum_{nlm} A_{nlm} \Phi_{nlm}(\mathbf{r}) \quad (1)$$

$$\rho(\mathbf{r}) = \sum_{nlm} A_{nlm} \rho_{nlm}(\mathbf{r}) \quad (2)$$

where  $\mathbf{r} \equiv (r, \phi, \theta)$  is expressed in spherical coordinates for convenience. We follow the derivation of Hernquist & Ostriker (1992) which used the Hernquist profile (Hernquist 1990) where  $\Phi_{000} \equiv -1/(1+r)$  and  $\rho_{000} \equiv 1/[2\pi r(1+r)^3]$  are the zeroth-order basis functions. The general basis functions can be written as

$$\Phi_{nlm} \propto -\frac{r^l}{(1+r)^{2l+1}} C_n^{(2l+3/2)}(\xi) Y_{lm}(\theta, \phi) \quad (3)$$

$$\rho_{nlm} \propto \frac{r^l}{r(1+r)^{2l+3}} C_n^{(2l+3/2)}(\xi) Y_{lm}(\theta, \phi) \quad (4)$$

where  $Y_{lm}$  are the spherical harmonics,  $C_n^{(\alpha)}(\xi)$  are the Gegenbauer polynomials, and  $\xi \equiv (r-1)/(r+1)$ . Taking advantage of the bi-orthonormality of the basis functions, each  $A_{nlm}$  can be computed based on a given  $\rho(\mathbf{r})$  by

$$A_{nlm} \propto \int \rho(\mathbf{r}) \Phi_{nlm}^*(\mathbf{r}) d\mathbf{r}. \quad (5)$$

The accelerations  $-\nabla\Phi$  can be obtained by differentiating Equation (1) analytically.

In practice, a snapshot from an N-body simulation contains  $\rho(\mathbf{r})$  which is represented by discrete particles, and the computations are much more easily done in real space. We refer the reader to Hernquist & Ostriker (1992) for a straightforward recipe to compute accelerations given a list of particle positions and masses. A

noteworthy feature of the SCF method is that all accelerations are proportional to the terms

$$\sum_{k=1}^N m_k \tilde{\Phi}_{nl}(r_k) P_{lm}(\cos\theta_k) \begin{bmatrix} \cos(m\phi_k) \\ \sin(m\phi_k) \end{bmatrix} \quad (6)$$

where  $m_k$  and  $(r_k, \theta_k, \phi_k)$  are the mass and position of the  $k$ th particle,  $\tilde{\Phi}_{nl}$  is the radial part of Equation (3), and  $P_{lm}$  are the Legendre polynomials. These linear summations over all  $N$  particles can be easily parallelized and precomputed given  $(n, l, m)$ . The decomposition is truncated at orders  $n_{max}$  and  $l_{max}$  (and  $m$  goes from 0 to  $l$  in real space), so both terms in Equation (6) are evaluated

$$\frac{n_{max}(l_{max} + 1)(l_{max} + 2)}{2} \quad (7)$$

times. After Equation (6) is precomputed, the accelerations can be obtained analytically.

A detailed strategy to parallelize the SCF method has been proposed by Hernquist et al. (1995) to compute N-body dynamics using the SCF method itself. Note that our problem is even simpler because we are only extracting the accelerations from an existing N-body snapshot, and the accelerations do not need to be propagated back to the bodies. The extracted accelerations serve as “external forces” for each particle of our stream simulations.

SCF offers a convenient way to account for redshift dependence. Since the model of one static potential is entirely represented by the set of coefficients  $A_{nlm}$  in Equation (1), these coefficients can simply be interpolated in redshift. L11 showed that the time variation of the first few coefficients at the lowest orders are relatively small, but higher-order variations may be more difficult to capture. However, this is unlikely to be a problem for us because we account for subhalos separately from the smooth halo. We defer the construction of a redshift-dependent potential to future studies.

## 2.2. Subhalo Finding

We use the AMIGA HALO FINDER<sup>1</sup> (AHF) to identify bound structures in the high-resolution region of VL-2. The most massive halo, hereafter the “main halo,” is the halo that hosts the subhalos and the tidal streams of interest in this study. Many particles in the main halo are also bound into additional levels of substructures. In the first level there are 11,523 “subhalos” that consist of at least 150 particles. The minimum halo mass threshold is chosen such that the average peak circular velocity for those halos ( $V_{max} \sim 2.5 \text{ km s}^{-1}$ ) approximately corresponds to the peak circular velocity below which the subhalo abundance is suppressed by numerical limitations (Diemand et al. 2008; Diemand & Moore 2011). This threshold choice allows for a robust sampling of the subhalo mass function.

In addition to each subhalo’s particle membership, AHF also automatically computes their intrinsic properties such as positions at the minimum potential, bulk velocities, scale radii, virial radii, etc. Table 1 summarizes the facts about our main halo, as well as the most and least massive subhalos. Note that the total number of particles and total mass of the main halo include all

TABLE 1  
MAIN HALO AND SUBHALOS IN THE  $z = 0$  SNAPSHOT OF VL-2.

Halo	$N$	$M$ ( $M_{\odot}$ )	$r_s$ (kpc)	$r_{vir}$ (kpc)
Main halo	$4.46 \times 10^8$	$1.89 \times 10^{12}$	60.4	400
Most massive subhalo	$1.15 \times 10^6$	$4.69 \times 10^9$	6.43	54.2
Least massive subhalo	150	$6.15 \times 10^5$	0.411	2.75

The total number of particles ( $N$ ), total masses ( $M$ ), scale radii ( $r_s$ ), and virial radii ( $r_{vir}$ ) of three nominal halos extracted by the halo finder, which found a total of 11,523 subhalos inside the virial radius of the main halo.

the particles of the subhalos, as returned by AHF. As we discuss in the following section, we remove the subhalo particles from the main halo, so the mass of the main halo in our simulations is slightly lower than the value stated in Table 1.

## 2.3. Modeling the smooth halo

In order to obtain a smooth halo from VL-2 that is a  $\Lambda$ CDM simulation, we remove all the subhalo particles from the main halo, leaving “voids” that were previously occupied by subhalos. When we construct the smooth halo’s potential, we use a low-order decomposition that only captures the overall shape of the main halo, but not the lumpiness due to the removed subhalos.

For convenience, for the smooth halo we only consider the cases where  $n_{max} = l_{max}$ , which we will refer to as the decomposition “order” collectively. Figures 1 and 2 show the accuracies of constructing the force field of the smooth halo using orders 10 and 20 by comparing against the force field that is obtained by directly summing up the force contributions from all the particles in the smooth halo. The force fields using both SCF and direct summation are computed in 94,747 randomly distributed positions inside a spherical shell of  $r = [15, 40]$  kpc in thickness where our stream will be orbiting.

There are 660 and 4620 terms in the decompositions using orders 10 and 20, respectively (Equation (7)). Figure 3 shows that the improvements in accuracy by increasing the order from 10 to 20 are marginal. For the purpose of this study, it is not necessary to model VL-2 with the highest possible accuracy. Our goal is to study the effects that a dark matter halo has on tidal streams in general, but not to model any particular objects that have been observed.

One alternative way to construct a smooth halo is to perform a decomposition with similar orders on all the main halo particles without removing the subhalo particles. We ran a similar analysis to Figures 1 and 2 using all particles, and we found that compared to having removed the subhalo particles, using all particles gave similar error levels except at positions near the subhalos, where the errors would typically be a few percent higher. This was expected because decompositions at orders 10 or 20 cannot model the forces inside the subhalos that were contributing to the directly summed forces. Removing the subhalo particles allowed us to confirm that our force errors were within 1% inside the smooth halo alone.

## 2.4. Adding Subhalos

For the lumpy halo, we now add the forces by the subhalos back into the smooth halo. We decompose each

<sup>1</sup> <http://popia.ft.uam.es/AHF/Download.html>

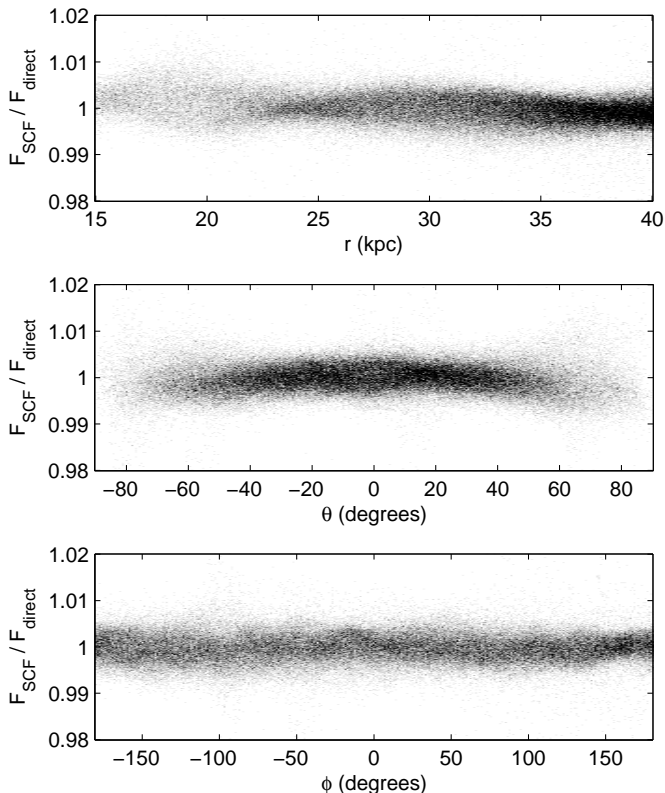


FIG. 1.— Comparing the magnitude of accelerations obtained from SCF ( $n_{max} = l_{max} = 10$ ) against directly summing up the accelerations from all particles in the smooth halo. The accelerations are measured at 94,797 randomly distributed positions inside a spherical shell of  $r = [15, 40]$  kpc. Top, middle, and bottom panels are the errors plotted against the  $(r, \theta, \phi)$  in spherical coordinates of the test positions. The accelerations are accurate to  $\sim 1\%$  level everywhere.

subhalo using  $n_{max} = 4, l_{max} = 0$ . In addition to being simpler to compute, we prefer not to decompose subhalos at higher orders because some low-mass subhalos can have only a few hundred particles, so a low  $n_{max}$  and spherically symmetric decomposition can avoid unphysical clumpiness in each subhalo. Also, subhalos' effects on tidal streams are expected to be of short duration, so it is not necessary to model individual subhalos in detail.

Adding subhalos separately to the smooth halo provides two advantages. First of all, we can control the mass range of subhalos that are present in the galaxy. This can be used to test theories such as warm dark matter that suppress the formation of low-mass subhalos. Also, each individual subhalo can orbit freely around the smooth halo, so their encounters with tidal streams can be modeled realistically.

Adding subhalos separately introduces extra mass to the smooth halo when comparing lumpy and smooth halos. Our full range of subhalos have masses  $1.067 \times 10^{11} M_{\odot}$  in total, which is about 6% of the mass of the smooth halo. In our simulations, we only use a subset of subhalos that (a) have pericentric distances of less than 40 kpc and (b) are less massive than  $10^8 M_{\odot}$ . The reason for requirement (a) is that subhalos that do not approach the stream will have minimal effects on our streams with apocentric distances at 30 kpc in their orbits. The reason for requirement (b) is that encounters with massive subhalos do not leave interesting signatures. As shown

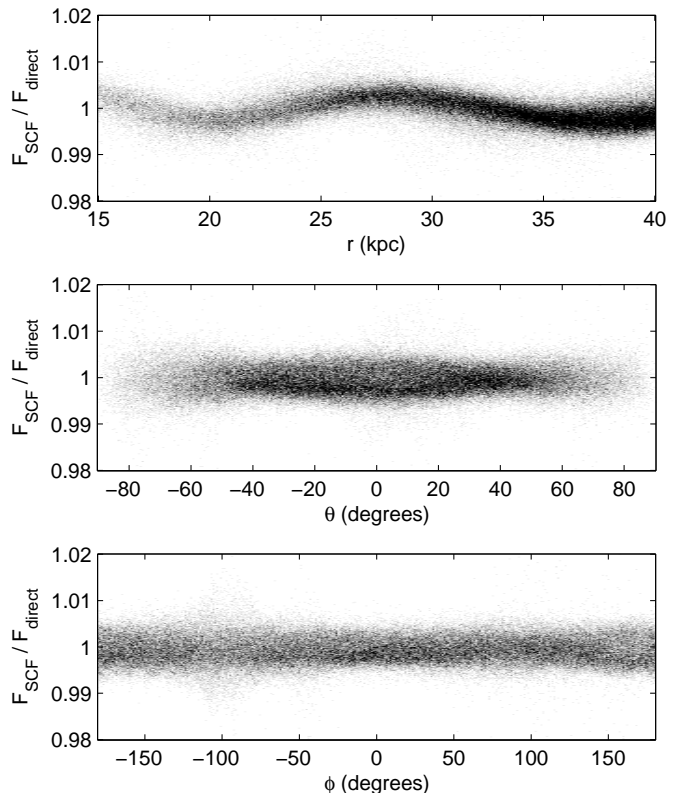


FIG. 2.— Same as Figure 1, but with  $n_{max} = l_{max} = 20$ . The top panel shows some correlation between the force error and radial position. This correlation is expected from basis functions whose radial components are polynomials. Nevertheless, the errors remain at the 1% level, so the correlation is not a concern.

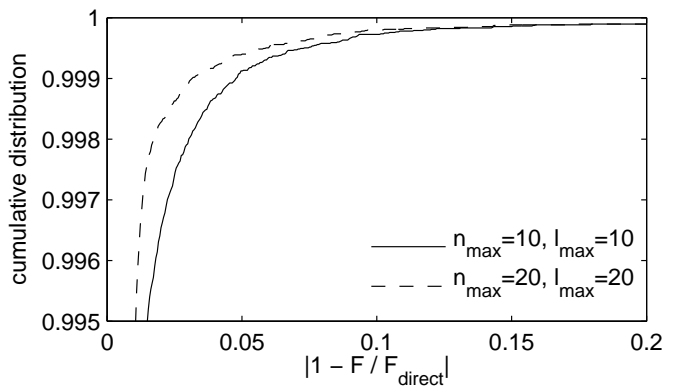


FIG. 3.— The cumulative distribution of the error at all the points in Figures 1 and 2. The  $\sim 1\%$  level error is achieved more than 99% of the time in both orders.

in Yoon et al. (2011), massive subhalos are rarer than low-mass subhalos, so massive subhalos mostly influence a stream by distant encounters that do not cause gaps in the stream. On the other hand, when a massive subhalo makes a close encounter with a stream, the effect is likely catastrophic to the stream as opposed to leaving small gaps that have been observed (Carlberg et al. 2012; Carlberg & Grillmair 2013). A separate study for the effects of massive subhalos on streams in a realistic potential is currently under way. For this study, after imposing requirements (a) and (b), the lumpy halo has 3808 subhalos in our simulations, which have a total mass of

$1.607 \times 10^{10} M_{\odot}$ , or about 1% of the mass of the smooth halo. Therefore, the streams simulated with and without subhalos will only have slightly different orbits, and the difference can be safely ignored for our comparisons.

### 3. STREAM SIMULATIONS

#### 3.1. Progenitor and Orbit

The streams’ progenitor is a star cluster following a King profile with core size 0.01 kpc and  $w = 4.91$ , where  $w$  can be thought of as the ratio between the depth of the potential and central velocity dispersion of the cluster. Its total mass is  $4.29 \times 10^4 M_{\odot}$ , central velocity dispersion is  $2.4 \text{ km s}^{-1}$ , and tidal radius is 0.103 kpc (identical to the one used in NC14). We use  $N = 1,000,000$  particles for the the main results of this study. Furthermore, as argued in NC14, the number of particles in the stream may be higher than the number of stars in the observed streams. Whether the effects we present in the following sections can be found in existing data requires more careful investigation, which is beyond the scope of this study.

We simulate the star cluster with two orbits shown in Figure 4 – both start at  $(x, y, z) = (30, 0, 0)$  kpc, but one orbit with  $(v_x, v_y, v_z) = (0, 120, 0) \text{ km s}^{-1}$  (“Orbit 1”), and the other with  $(0, 41.0, 113) \text{ km s}^{-1}$  (“Orbit 2”), which is the former with an initial velocity inclined at  $70^\circ$  from the  $xy$ -plane. The VL-2 main halo has not been aligned with any axis, so the directions of the initial velocities are arbitrarily chosen to explore the main halo as much as possible. Although neither orbit is confined in any orbital planes, both are tube orbits with apo- and pericentric distances at roughly  $\sim 30$  kpc and  $\sim 17$  kpc, which are chosen to be similar to the inferred values of the GD-1 stream (Grillmair & Dionatos 2006; Willett et al. 2009).

#### 3.2. Simulation Details

The SCF decomposition is performed using the procedure exactly described in Hernquist & Ostriker (1992). Since we consider decomposition orders that are much lower than the number of particles in VL-2, it is not necessary to apply a smoothening kernel to the VL-2 particles when computing the decomposition coefficients because a low-order decomposition, by construction, cannot capture the granularity of the VL-2 particles.

Our N-body simulations of streams are computed using GADGET-2 (Springel 2005), which is available to the public<sup>2</sup>. We modify GADGET-2 so it uses the precomputed SCF decomposition coefficients to construct the external accelerations, which are added to the particles in our stream simulations after the stream particles’ N-body forces have been computed. We impose a maximum time step of 1 Myr and softening of 5 pc for the particles so that they are essentially collisionless.

## 4. RESULTS AND DISCUSSION

### 4.1. Decomposition Order

#### 4.1.1. Orbital Convergence

The basis functions in the SCF method are complete, which means that the higher the decomposition order,

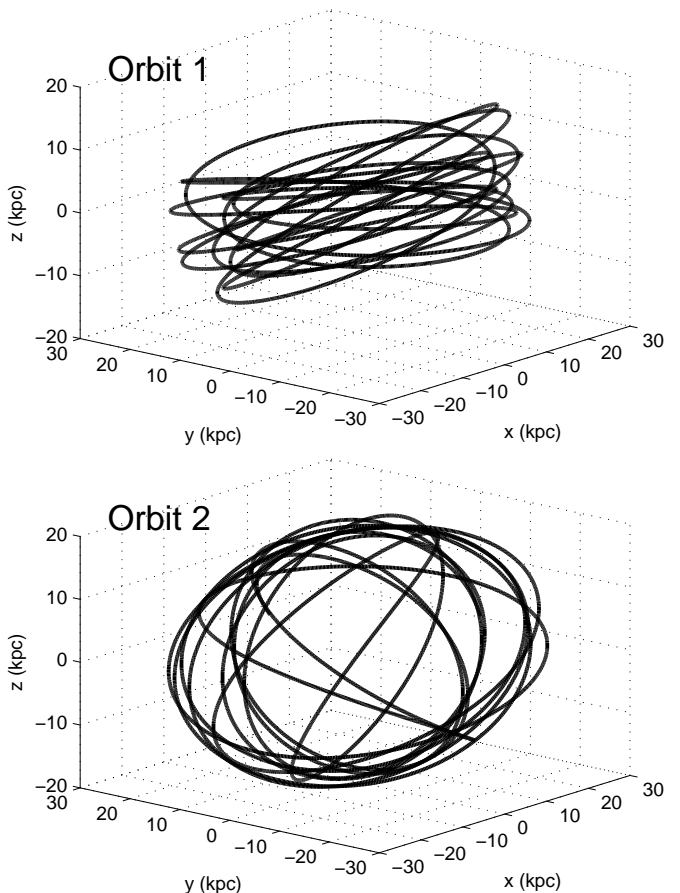


FIG. 4.— Two stream orbits in an SCF potential of the smooth halo using order 10 with initial positions at  $(x, y, z) = (30, 0, 0)$  kpc, but with  $(v_x, v_y, v_z) = (0, 120, 0) \text{ km s}^{-1}$  (“Orbit 1”; top panel) and  $(0, 41.0, 113) \text{ km s}^{-1}$  (“Orbit 2”; bottom panel). Both are tube orbits with apo- and pericenters that roughly correspond to the inferred values of GD-1.

the more accurate the constructed model will be. It is crucial to understand the decomposition order necessary for our purposes. Neither VL-2 nor our stream simulations are meant to be physical models of any observations, so it is not necessary for us to model the VL-2 main halo to the highest possible accuracy with a high decomposition order. In fact, since we have removed subhalos from the main halo, modeling these “voids” in the smooth halo may result in spurious forces. On the other hand, if the decomposition order is too low, then it compromises the value in using VL-2, which features shapes and profiles missing in idealized profiles. We require a decomposition order that is high enough to capture the shape and profile of the VL-2 smooth halo, but not high enough to capture the granularity of its substructures (the contribution by substructures will be added in after the smooth halo has been modeled).

The radial coordinates of the two stream orbits as functions of time for various decomposition orders are shown in Figure 5. Both orbits have converged to within a few percent everywhere for 10 Gyr. This is expected from Figures 1 and 2, which show that the forces almost everywhere are accurate to  $\sim 1\%$  even at only order 10. Therefore, a decomposition order 10 is sufficient for our purposes. Using order 10 has the advantage that subhalo “voids” will not be captured. There are more than 10,000

<sup>2</sup> <http://www.mpa-garching.mpg.de/gadget/>

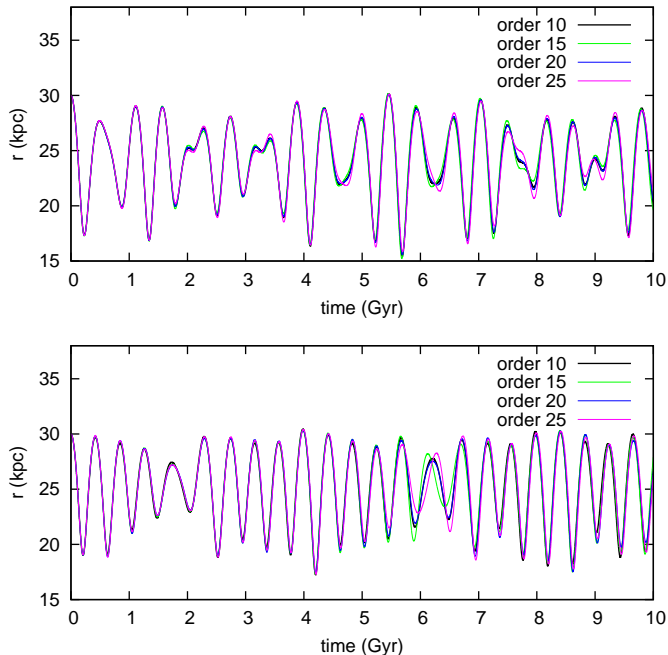


FIG. 5.— Radial coordinates of two stream orbits shown in Figure 4. Top and bottom panels show Orbits 1 and 2, respectively. These two plots show that their orbits have converged at order 10.

subhalos found within the virial radius of the main halo, and the granularities of these subhalos cannot be modeled by polynomials of only the 10th degree in either the radial or angular components of SCF basis functions.

L11 showed that decompositions lower than order 10 give significant errors in the region less than a few kiloparsecs away from the halo’s center, so L11 adapted order 20 to suppress those errors. That region is not relevant for our streams because they orbit at galactocentric distances well beyond a few kiloparsecs. Nevertheless, our convergence results agree with L11, which showed that the acceleration errors compared to direct summation are at  $\sim 1\%$  beyond 17 kpc, and that increasing from order 9 to 19 provides minimal gain at those regions.

#### 4.1.2. Stream Density Convergence

As shown in NC14, signatures of subhalos can be detected in the linear density, or number of particles per unit length, along the stream. Even though the previous sections show that the accelerations and orbits have converged to within a few percent, we now investigate how well the stream density converges.

Figure 6 shows the linear density along four streams using 100,000 particles each and traced along a sky projection as seen by an observer at the galactic center (so the unit along the length of stream is angular) at 6.7 Gyr. The four streams started with identical progenitors in Orbit 1, but in the smooth halos that are constructed using orders 10, 15, 20, and 25. Although the overall profiles of the streams’ densities on large scales are similar among the four orders, the detailed fluctuations are quite different. To investigate the significance of these differences, we simulated a few additional streams with different random realizations of the progenitor, but with the same number of particles, physical parameters, and orbit, in the same smooth halo potential using or-

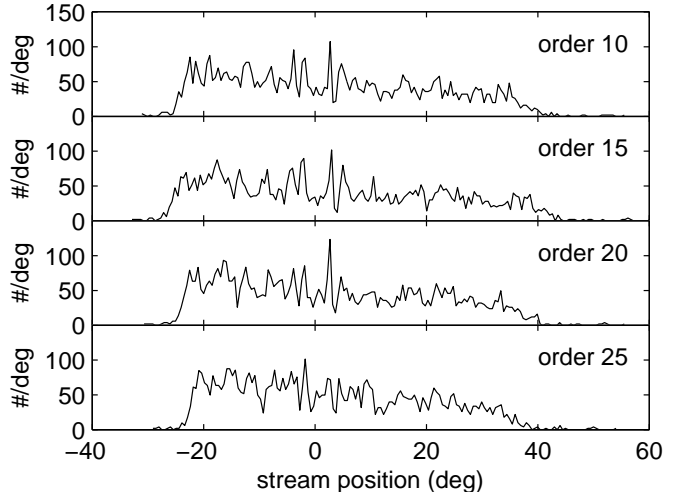


FIG. 6.— Four streams that start with the same initial conditions with Orbit 1 in the smooth halo that is constructed using different decomposition orders. The streams’ overall profiles on large scales are similar, but the density fluctuations on small scales are different.

der 10. We find that the small-scale differences between these additional streams are indistinguishable from the differences between the four panels in Figure 6. Therefore, the differences shown in the figure are simply due to stochastic noise of the particles, and our decomposition has sufficiently converged at order 10.

The convergence of our decomposition can also be seen in Figure 7, which shows the mass loss for each stream in Figure 6. Every large spike, or major mass loss event, in each stream is associated with a pericentric passage shown in the top panel of Figure 5. However, the minor mass-loss events do not occur at the same rate among the four orders. Our additional streams with different progenitor realizations as explained above show, again, that the small-scale differences for each decomposition order shown in Figure 7 are indistinguishable from stochastic noise.

We adapt order 10 for the smooth halo for the rest of our results. As we show in the next sections, gaps caused by subhalos are longer than the spurious gaps caused by changing the decomposition order as shown in Figure 6. This is similar to the result of NC14, where the gap size distribution can be used to distinguish “intrinsic” gaps from subhalo gaps. In the future, we aim to repeat similar analyses to NC14 using various SCF decomposition orders for the realistic halo.

## 4.2. Densities along the Streams

### 4.2.1. Stream 1 in the Smooth Halo

We first examine the intrinsic features in the stream in Orbit 1 (hereafter “Stream 1”) in the smooth halo without any subhalos. Figure 8 shows the surface density of the stream projected on the sky from 8 to 8.5 Gyr as seen by an observer situated at the galactic center, and Figure 9 shows the linear density along the stream at the same times. This time frame roughly corresponds to one radial oscillation (though it is not a “radial period”; see Figure 5), so it allows us to investigate the streams’ features as the streams stretch and compress during that oscillation.

The resulting stream is long and narrow, with a

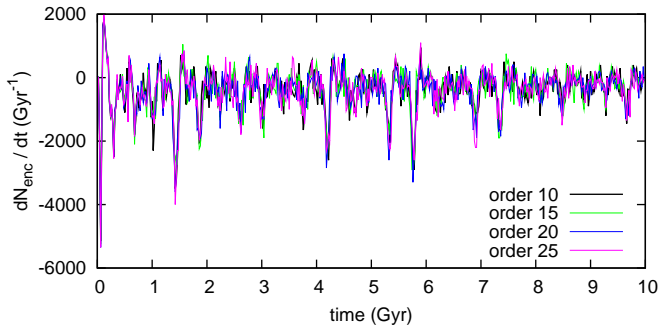


FIG. 7.— Rate of change in the number of particles enclosed in 0.1 kpc from the center of the progenitor as a function of time in Orbit 1. Every spike in mass loss is associated with a pericentric passage. Even though the major mass loss events occur at the same time at the same rate among all orders, the minor events do not.

length-to-width ratio of about 50 (which is slightly lower than the observed values in GD-1 (Grillmair & Dionatos 2006)), so it can simply be represented by its linear density. The most prominent feature in the linear density is the spikes located within  $10^\circ$  away from either side of the progenitor. Upon inspection, we find that new spikes develop immediately after pericentric passages, and each spike originates from the progenitor and migrates toward the ends of the stream. One possible cause of the density spikes is EOs, which are caused by the “piling up” of particles in their epicyclic orbits as they escape from the progenitor. In the original derivations in Küpper et al. (2008, 2010), the spacings between the EOs are calculated assuming an axisymmetric potential. Although the VL-2 halo has no spatial symmetry, we can approximate it by spherically averaging our potential model (ie. taking  $l_{max} = 0$  in Equation (1)). Using a representative value of  $R$  for the angular frequency  $\Omega$  and epicyclic frequency  $\kappa$ , we can estimate the spacing

$$|y_C| = \frac{4\pi\Omega}{\kappa} \left(1 - \frac{4\Omega^2}{\kappa^2}\right) x_L, \quad (8)$$

where  $x_L = GM/(4\Omega^2 - \kappa^2)$ , between the first EOs on either branch of the stream (Küpper et al. 2008). For  $R = 24$  kpc (roughly the galactocentric radius of the progenitor at 8.3 Gyr), we obtain  $\Omega \simeq 8 \text{ Gyr}^{-1}$  and  $\kappa \simeq 12 \text{ Gyr}^{-1}$ . This gives  $|y_C| \simeq 0.77$  kpc, or  $1.8^\circ$  when projected onto the sky, which is almost a factor of 2 smaller than the measured spacing at  $\sim 3^\circ$  between the first two density spikes at 8.3 Gyr. Note that as the stream compresses and stretches as it oscillates radially, the spacing between the spikes can easily differ by factors of a few (eg. compare 8.2 and 8.4 Gyr in Figure 9).

The density profiles along the stream shown in Figure 9 indicate that the density spikes near the progenitor are very prominent inside the VL-2 potential and are similar to those in NC14 in a spherical potential – they are regularly spaced and appear very close to the progenitor. As we shall see in the next sections, gaps caused by subhalos are randomly spaced and can occur anywhere along the stream.

#### 4.2.2. Stream 1 in the Lumpy Halo

Figures 10 and 11 show the sky projection and linear density of Stream 1 in a lumpy halo with 3807 subhalos. Compared to the same stream in the smooth halo, the

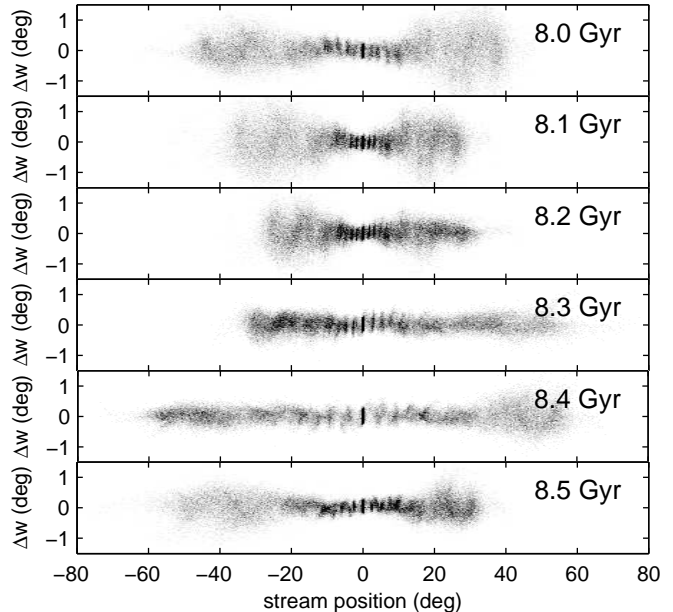


FIG. 8.— Sky-projected surface density of the stream in Orbit 1 in the smooth halo. The projection is seen from a hypothetical observer situated in the galactic center. Since the stream is extremely narrow compared to the size of its orbit, the curvature of the stream on the sky has been subtracted, and the progenitor has been shifted to have position at  $0^\circ$ . Note that the width of the stream ( $\Delta w$  on the y-axis) is about 50 times smaller than the length of the stream.

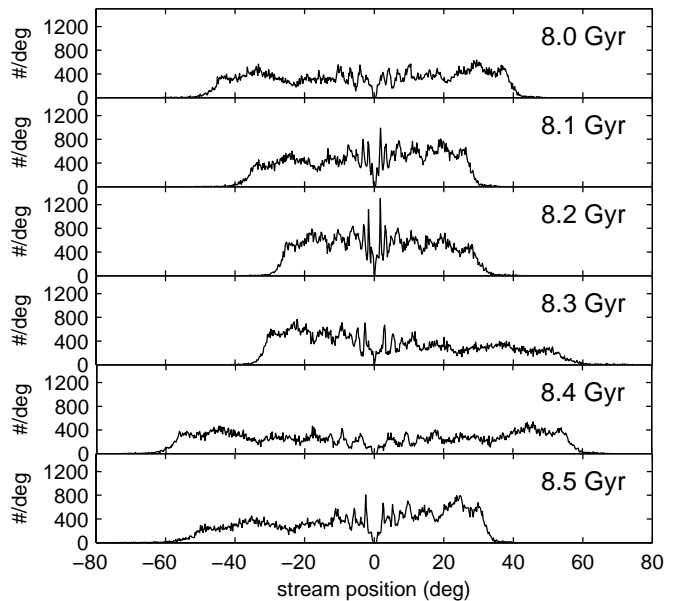


FIG. 9.— Linear density corresponding to the same stream shown in Figure 8. The progenitor at position  $0^\circ$  has been masked out. Epicyclic overdensities appear as the first few spikes within about  $10^\circ$  on either side of the progenitor (especially noticeable at 8.2 Gyr when the stream is compressed).

density clearly shows gaps as local minima that are more pronounced and occur everywhere along the stream. The density spikes near the progenitor are still present with similar spacing to the stream in the smooth halo. This is not surprising, since the extra subhalos contribute only  $\sim 1\%$  of the total mass of the smooth halo, so any effects due to the stream’s orbit would not be different from the

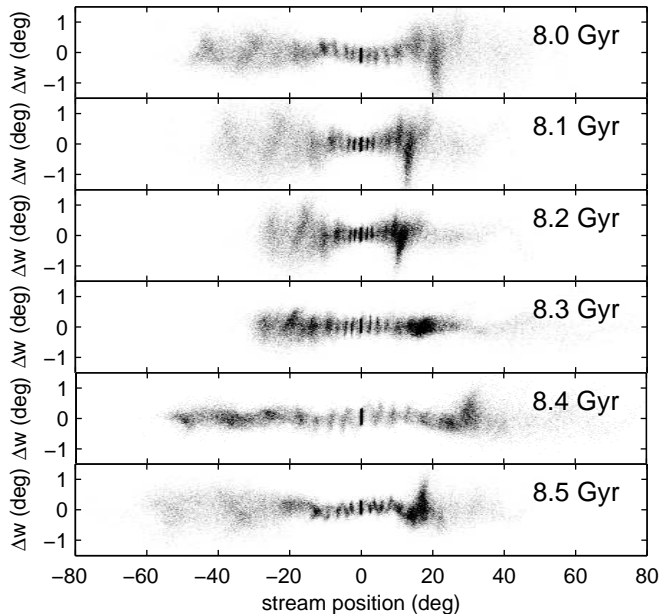


FIG. 10.— Same as Figure 8, but in a lumpy halo with 3807 subhalos.

smooth halo case.

Recall from Section 2.4 that our simulations in the lumpy halo contains 3808 subhalos. An interesting but rare event that occurred in the simulation with 3808 subhalos was that the progenitor had a close encounter at less than one half-mass radius from a  $1.8 \times 10^7 M_\odot$  subhalo at an early time, which caused a sudden burst in mass loss for the progenitor. This resulted in a stream that was dominated by two large but smooth spikes, one in each branch of the stream. When this subhalo was eliminated, we were able to resolve the density fluctuations caused by close encounters between the tidal tails and subhalos as shown in Figures 10 and 11, rather than between the progenitor and subhalos. In the future we aim to study the probability that a progenitor or its tidal stream becomes catastrophically perturbed by subhalos in the VL-2 halo.

#### 4.2.3. Stream 2 in the Smooth Halo

Figure 12 shows the sky-projected density of the stream in Orbit 2 (hereafter “Stream 2”) from 6.0 to 6.7 Gyr in the smooth halo. Similar to our investigation for Stream 1, this time frame also covers roughly one radial oscillation even though a well-defined radial period does not exist in the VL-2 potential (Figure 5). Compared to Stream 1, Stream 2 becomes “fluffy” at the far ends of its tidal tails, with widths sometimes comparable to the length of the narrow part of the stream. This is very different from Stream 1 shown in Figure 8, which has a high length-to-width ratio throughout.

An important implication is that only the narrow segment of the stream may be dense enough to be observable, and the rest of the stream may be too diffuse. Simulations in Pearson et al. (2015) in triaxial potentials also showed similarly diffuse features dubbed “stream-fanning” in the tips of tidal tails, which are not found in observations. The physical origin of stream-fanning has yet to be understood and is beyond the scope of our study, so it is not clear whether our Stream 2 is exhibiting

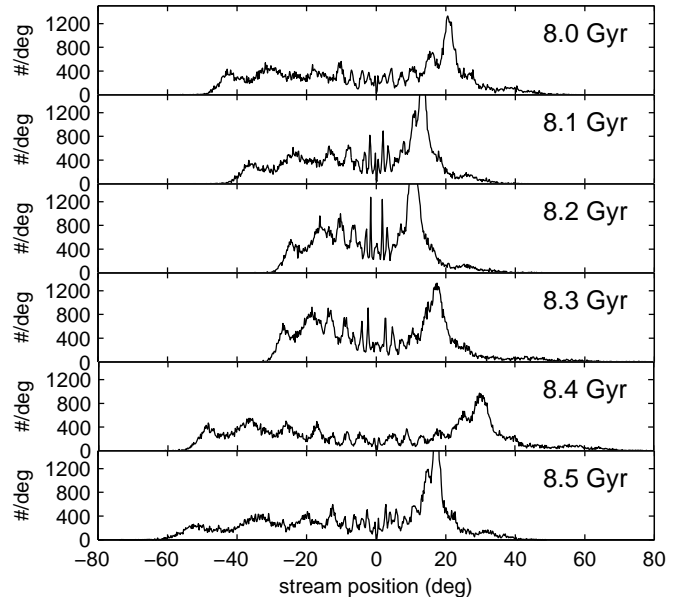


FIG. 11.— Linear density corresponding to the same stream shown in Figure 10. Compared to the smooth halo case (Figure 9), in a lumpy halo the stream appears clumpier with more local minima in density everywhere in the tails of the stream.

stream-fanning.

Because of the diffuse tails, it is no longer appropriate to analyze the entire stream simply by the linear density. Nevertheless, we can trace the linear density along the narrow part of the stream out to about  $10^\circ$ – $20^\circ$  away from the progenitor. Figure 13 shows the densities along the stream at each time shown in Figure 12. The density profiles show prominent density spikes next to the progenitor, and the spacings between those spikes are in rough agreement with the derivation in Section 4.2.1. Other than this, the density profiles fall off very quickly and smoothly toward the diffuse ends of the stream.

#### 4.2.4. Stream 2 in the Lumpy Halo

Figure 14 shows the sky-projected density of Stream 2 from 6.0 to 6.7 Gyr in a lumpy halo with 3808 subhalos. The stream resembles the case in the smooth halo (Figure 12) with very fluffy ends, but in a lumpy halo they are even more prominent. In the fluffy regions the width can exceed the length of the narrow regions, which span only  $10^\circ$ – $20^\circ$ .

The linear density along the stream can be plotted, but similar to the case in the smooth halo, it is only appropriate to the narrow regions near the progenitor. As seen in Figure 15, the density profiles in those regions are also smooth with the exception of the first or second density spikes. Therefore, for this stream, there are no distinguishable signatures in the linear density that traces the existence of subhalos.

Perhaps a more interesting aspect of this stream is the tips of its tidal tails. The wide and diffuse tails shown in Figure 14 are reminiscent of “shell”-like features found in satellite systems that plunge near the galactic center on very eccentric orbits. With apo- and pericentric distances at  $r_a \simeq 30$  kpc and  $r_p \simeq 17$  kpc, respectively, the stream’s eccentricity is  $e = (r_a - r_p)/(r_a + r_p) \simeq 0.3$ . This implies that satellites do not need to be on eccentric orbits to have significant parts of their tidal tails disrupted

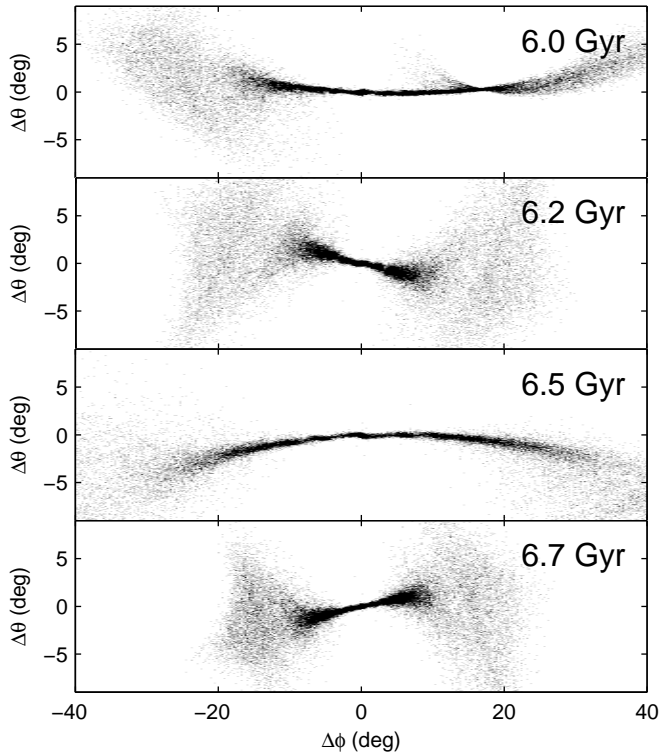


FIG. 12.— Sky-projected surface density of Stream 2 in the smooth halo. The projection is seen from a hypothetical observer situated in the galactic center. Compared to Figure 8, the streams here contain diffuse ends sometimes as wide as the length of the stream. Rather than tracing a line and subtracting their curvatures on the sky, the streams shown here are simply shifted so that the progenitors have  $\phi = \theta = 0$ , and then rotated so they appear roughly horizontal.

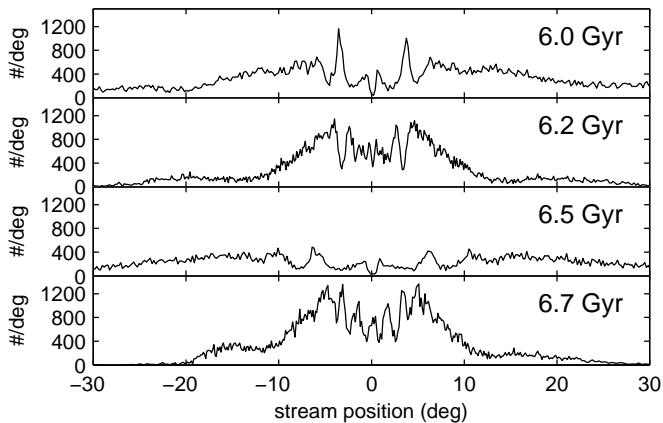


FIG. 13.— Linear density corresponding to the same stream shown in Figure 12. A line has only been traced along the regions up to  $20^\circ$  away from the progenitor. The progenitor at position  $0^\circ$  has been masked out. The density profiles show prominent density spikes near the progenitor, similar to Stream 1, but the profiles quickly fall off to the diffuse regions without many intrinsic features.

such that their surface brightnesses may be even lower than that of the narrow stream itself, which is already difficult to observe. In NC14, the same progenitor orbiting a spherical and idealized halo with similar eccentricity to Streams 1 and 2 here could only produce a narrow stream. This indicates that using a realistic halo is important when studying the effects that subhalos have on

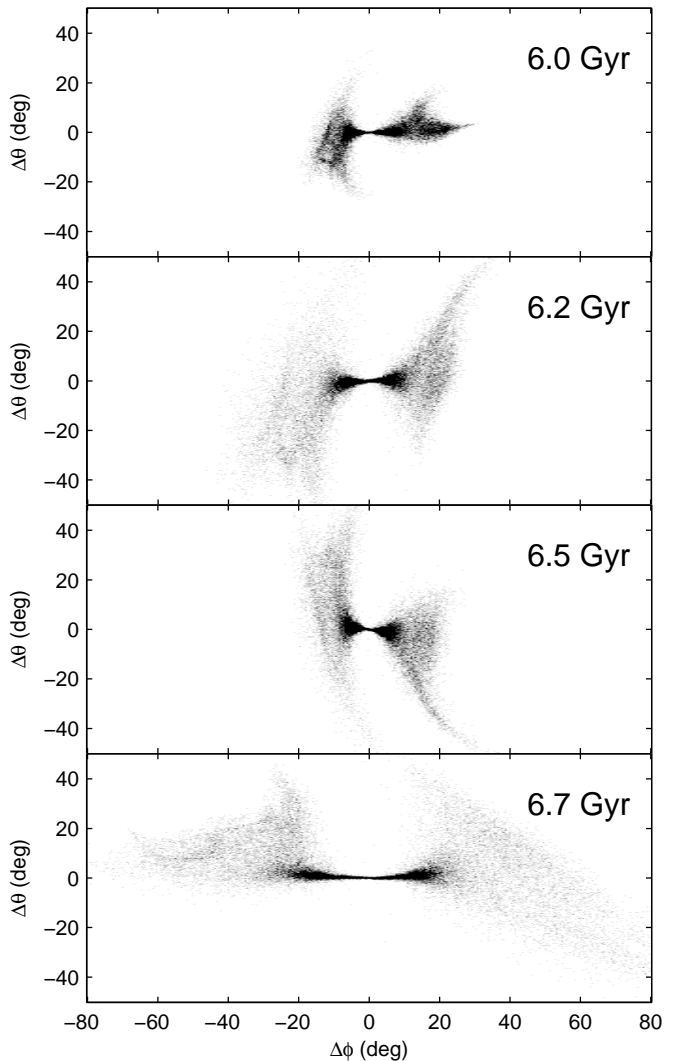


FIG. 14.— Same as Figure 12, but in the lumpy halo. The stream overall appears similar to the case in the smooth halo, but the diffuse ends of the stream are even more prominent, and sometimes even wider than the narrow part of the stream itself.

GD-1-like streams. In a future study, we aim to simulate the tidal disruptions of globular-cluster type satellites in many orbits in both the smooth and lumpy halos in order to study the survival rate of tidal tails.

## 5. SUMMARY AND CONCLUSION

We constructed potential models using the high-resolution dark matter halo in the  $z = 0$  snapshot of the Via Lactea II (VL-2) simulation. In the high-resolution “main” halo, we used a halo finder to remove and isolate subhalo particles. The potentials of the main halo and the subhalos were then constructed individually. This allowed us to simulate tidal streams in the main halo with and without subhalos. We investigated the difference in the stream between the two cases and showed that, even in a realistic potential without using idealized profiles, streams remain a valuable probe to detect subhalos whose existence is a crucial prediction of the  $\Lambda$ CDM model.

The SCF method (Hernquist & Ostriker 1992) has previously been applied to the Aquarius simulations (Springel et al. 2008; Lowing et al. 2011) as a tool to

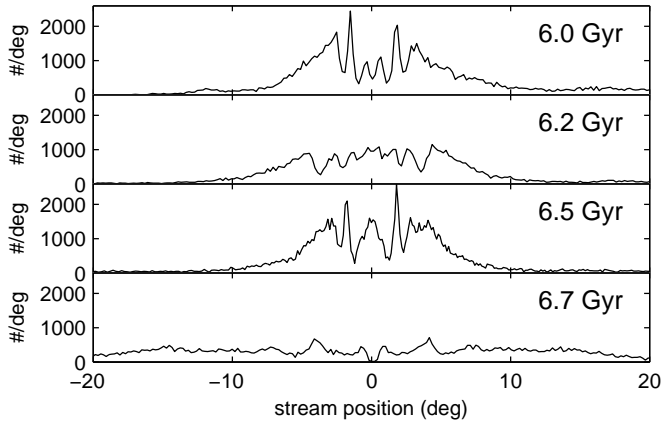


FIG. 15.— Linear density corresponding to the same stream shown in Figure 14. Similar to the case in the smooth halo, linear density is only appropriate at the regions near the progenitor where the stream is narrow. Aside from the density spikes near the progenitor, the density profile is smooth and featureless.

study dynamics inside existing high-resolution simulations of dark matter halos. For the first time, we applied it to the VL-2 simulation to examine the subhalos’ dynamical influence on tidal streams. The SCF method is a powerful and parallelizable method that efficiently computes the potential to arbitrary accuracy using a set of complete and bi-orthonormal basis functions.

The potentials in the main halo and all the subhalos were constructed using the SCF method. When the subhalo particles were removed from the main halo, the main halo’s potential was constructed using an order 10 decomposition to ensure that the main halo remained smooth and contained no granularities due to the removal of its subhalos. After the subhalos’ individual potentials were also constructed, they were added to the smooth halo in orbits with the initial positions and velocities as found by the halo finder. This eliminated the need for any assumptions for the profiles and distributions for the subhalos in the lumpy halo.

We simulated the tidal disruption of a star cluster as an N-body system that used the main halo’s and subhalos’ potentials as external forces. The cluster followed two orbits, one with initial velocity with zero  $z$  component (“Stream 1”), and another with the same speed but inclined from the  $xy$ -plane by  $70^\circ$  (“Stream 2”). In a potential without spatial symmetry, neither orbit was confined to any orbital planes, but both orbits were chosen to have apo- and pericentric distances at about 30 and 17 kpc, respectively. These values are comparable to the inferred orbit of GD-1 from observations (Grillmair & Dionatos 2006; Willett et al. 2009). We simulated each stream in both the smooth halo and the lumpy halo.

Stream 1 remained narrow for 10 Gyr, with length-to-width ratio  $\simeq 50$ , which was comparable to the observations of GD-1. Even though the smooth halo had no spatial symmetry, we still found density spikes that were similar to EOs near the stream progenitor. In the smooth halo, there were density fluctuations along the stream that were not found in a spherical halo, but the fluctuations were not as prominent as the ones found in the stream in the same orbit but in a lumpy halo. In the future we aim to repeat analyses similar to Ngan & Carlberg (2014), which used gap size distributions to distinguish “intrinsic” gaps and subhalo gaps in streams. Since gap size distributions are observable (Carlberg & Grillmair 2013), understanding them for simulated streams in a realistic halo is an essential step for comparing simulations and observations.

Stream 2 was narrow only up to  $10^\circ$ – $20^\circ$  away from the progenitor as seen by a hypothetical observer situated at the galactic center. Further along the stream from the narrow part, the stream developed fluffy features that were almost as wide as, if not wider than, than the length of the narrow part of the stream. We found that density spikes, similar to the ones in Stream 1, near the progenitor dominated the linear density along the narrow part without any distinguishable signatures of subhalos. However, in the lumpy halo, the stream featured wider and even more diffuse tails than in the smooth halo. This means that in the lumpy halo the stream may be even more difficult to observe than in the smooth halo.

Dynamics in the VL-2 halo potential is beyond the scope of this study. In this study we used only two streams in two arbitrary but similar orbits to illustrate the VL-2 halo’s complexity compared to idealized and spherical halo models that were used in previous studies (Yoon et al. 2011; Carlberg 2013; Ngan & Carlberg 2014). In a spherical halo, our two streams in this study would appear identical and would not reveal the complicated morphologies especially demonstrated by Stream 2. In the future, we aim to use this VL-2 model to simulate more streams in more orbits and to perform much more detailed analysis to each stream.

B.B., R.W., and A.S. are supported by NSF grant OIA-1124403, and P.M. by OIA-1124452. We thank the anonymous referee for a constructive report. W.N. also thanks John Dubinski for useful discussions for the SCF method. Computations were performed on the GPC supercomputer at the SciNet HPC Consortium. SciNet is funded by the Canada Foundation for Innovation under the auspices of Compute Canada; the Government of Ontario; Ontario Research Fund - Research Excellence; and the University of Toronto.

## REFERENCES

- Bardeen, J. M., Bond, J. R., Kaiser, N., & Szalay, A. S. 1986, *ApJ*, 304, 15
- Blumenthal, G. R., Faber, S. M., Primack, J. R., & Rees, M. J. 1984, *Nature*, 311, 517
- Bonaca, A., Geha, M., Küpper, A. H. W., et al. 2014, *ApJ*, 795, 94
- Carlberg, R. G. 2012, *ApJ*, 748, 20
- . 2013, *ApJ*, 775, 90
- Carlberg, R. G., & Grillmair, C. J. 2013, *ApJ*, 768, 171
- Carlberg, R. G., Grillmair, C. J., & Hetherington, N. 2012, *ApJ*, 760, 75
- Carlberg, R. G., Richer, H. B., McConnachie, A. W., et al. 2011, *ApJ*, 731, 124
- Comparetta, J., & Quillen, A. C. 2011, *MNRAS*, 414, 810
- Davis, M., Efstathiou, G., Frenk, C. S., & White, S. D. M. 1985, *ApJ*, 292, 371
- Diemand, J., Kuhlen, M., & Madau, P. 2007, *ApJ*, 657, 262
- Diemand, J., Kuhlen, M., Madau, P., et al. 2008, *Nature*, 454, 735
- Diemand, J., & Moore, B. 2011, *Advanced Science Letters*, 4, 297

- Erkal, D., & Belokurov, V. 2014, ArXiv e-prints, arXiv:1412.6035
- Gao, L., Frenk, C. S., Boylan-Kolchin, M., et al. 2011, MNRAS, 410, 2309
- Grillmair, C. J., & Dionatos, O. 2006, ApJ, 643, L17
- Helmi, A., White, S. D. M., & Springel, V. 2003, MNRAS, 339, 834
- Hernquist, L. 1990, ApJ, 356, 359
- Hernquist, L., & Ostriker, J. P. 1992, ApJ, 386, 375
- Hernquist, L., Sigurdsson, S., & Bryan, G. L. 1995, ApJ, 446, 717
- Ibata, R. A., Lewis, G. F., Irwin, M. J., & Quinn, T. 2002, MNRAS, 332, 915
- Jing, Y. P., & Suto, Y. 2002, ApJ, 574, 538
- Johnston, K. V. 1998, ApJ, 495, 297
- Klypin, A., Kravtsov, A. V., Valenzuela, O., & Prada, F. 1999, ApJ, 522, 82
- Küpper, A. H. W., Kroupa, P., Baumgardt, H., & Heggie, D. C. 2010, MNRAS, 401, 105
- Küpper, A. H. W., Lane, R. R., & Heggie, D. C. 2012, MNRAS, 420, 2700
- Küpper, A. H. W., MacLeod, A., & Heggie, D. C. 2008, MNRAS, 387, 1248
- Law, D. R., Johnston, K. V., & Majewski, S. R. 2005, ApJ, 619, 807
- Law, D. R., Majewski, S. R., & Johnston, K. V. 2009, ApJ, 703, L67
- Lowing, B., Jenkins, A., Eke, V., & Frenk, C. 2011, MNRAS, 416, 2697
- Madau, P., Diemand, J., & Kuhlen, M. 2008, ApJ, 679, 1260
- Moore, B., Ghigna, S., Governato, F., et al. 1999, ApJ, 524, L19
- Navarro, J. F., Frenk, C. S., & White, S. D. M. 1997, ApJ, 490, 493
- Navarro, J. F., Hayashi, E., Power, C., et al. 2004, MNRAS, 349, 1039
- Navarro, J. F., Ludlow, A., Springel, V., et al. 2010, MNRAS, 402, 21
- Ngan, W. H. W., & Carlberg, R. G. 2014, ApJ, 788, 181
- Pearson, S., Küpper, A. H. W., Johnston, K. V., & Price-Whelan, A. M. 2015, ApJ, 799, 28
- Siegal-Gaskins, J. M., & Valluri, M. 2008, ApJ, 681, 40
- Springel, V. 2005, MNRAS, 364, 1105
- Springel, V., Wang, J., Vogelsberger, M., et al. 2008, MNRAS, 391, 1685
- Stadel, J., Potter, D., Moore, B., et al. 2009, MNRAS, 398, L21
- Strigari, L. E., Bullock, J. S., Kaplinghat, M., et al. 2007, ApJ, 669, 676
- Willett, B. A., Newberg, H. J., Zhang, H., Yanny, B., & Beers, T. C. 2009, ApJ, 697, 207
- Yoon, J. H., Johnston, K. V., & Hogg, D. W. 2011, ApJ, 731, 58
- Zemp, M. 2009, Modern Physics Letters A, 24, 2291
- Zemp, M., Diemand, J., Kuhlen, M., et al. 2009, MNRAS, 394, 641